Current Research in Neurobiology 3 (2022) 100062

Contents lists available at ScienceDirect

Current Research in Neurobiology

journal homepage: www.sciencedirect.com/journal/current-research-in-neurobiology

Murine model of triosephosphate isomerase deficiency with anemia and severe neuromuscular dysfunction

Tracey D. Myers [a,b,c], Carolyn Ferguson [d], Eric Gliniak [b,c], Gregg E. Homanics [a,b,d,e], Michael J. Palladino [a,b,c,*]

[a] Center for Neuroscience, University of Pittsburgh, Pittsburgh, PA, USA
[b] Department of Pharmacology and Chemical Biology, University of Pittsburgh, Pittsburgh, PA, USA
[c] Pittsburgh Institute for Neurodegenerative Diseases, University of Pittsburgh, Pittsburgh, PA, USA
[d] Department of Anesthesiology and Preoperative Medicine, University of Pittsburgh, Pittsburgh, PA, USA
[e] Department of Neurobiology, University of Pittsburgh, Pittsburgh, PA, USA

ARTICLE INFO

Keywords:
Triosephosphate isomerase (TPI)
TPI Deficiency
CRISPR
Genetics
Glycolysis
Metabolism

ABSTRACT

Triosephosphate isomerase deficiency (TPI Df) is a rare, aggressive genetic disease that typically affects young children and currently has no established treatment. TPI Df is characterized by hemolytic anemia, progressive neuromuscular degeneration, and a markedly reduced lifespan. The disease has predominately been studied using invertebrate and *in vitro* models, which lack key aspects of the human disease. While other groups have generated mammalian *Tpi1* mutant strains, specifically with the mouse *mus musculus,* these do not recapitulate key characteristic phenotypes of the human disease. Reported here is the generation of a novel murine model of TPI Df. CRISPR-Cas9 was utilized to engineer the most common human disease-causing mutation, $Tpi1^{E105D}$, and $Tpi1^{null}$ mice were also isolated as a frame-shifting deletion. $Tpi1^{E105D/null}$ mice experience a markedly shortened lifespan, postural abnormalities consistent with extensive neuromuscular dysfunction, hemolytic anemia, pathological changes in spleen, and decreased body weight. There is a ~95% reduction in TPI protein levels in $Tpi1^{E105D/null}$ animals compared to wild-type littermates, consistent with decreased TPI protein stability, a known cause of TPI Df. This work illustrates the capability of $Tpi1^{E105D/null}$ mice to serve as a mammalian model of human TPI Df. This work will allow for advancement in the study of TPI Df within a model with physiology similar to humans. The development of the model reported here will enable mechanistic studies of disease pathogenesis and, importantly, efficacy testing in a mammalian system for emerging TPI Df treatments.

1. Introduction

Triosephosphate isomerase (TPI) is a glycolytic enzyme responsible for interconverting glyceraldehyde-3-phosphate (G3P) and dihydroxyacetone phosphate (DHAP). The conversion of DHAP into G3P is essential for achieving the full energetic yield of glycolysis, since only G3P proceeds through the rest of the glycolytic pathway. Reduction in TPI levels results in a progressive multi-system degenerative disorder called TPI Deficiency (TPI Df) (Schneider et al., 1965). TPI Df is a rare fully recessive metabolic disorder characterized by progressive muscle degeneration, neurological dysfunction, hemolytic anemia, and markedly reduced longevity (Orosz et al., 2006). There are currently fewer than 20 known patients living with the disease in the world. Patients are typically diagnosed in early childhood and the disease is often fatal within 5 years of diagnosis. The most common cause of death is respiratory failure, and ventilators are often utilized in late-stage disease. Aside from supportive care, there are currently no effective treatments for this debilitating and aggressive disease, though the ketogenic diet may provide some benefit (Fogle et al., 2019).

TPI Df is an autosomal recessive disease commonly caused by a homozygous missense mutation in the *TPI1* gene leading to a single amino acid substitution, glutamate to an aspartate at the 105th codon

Abbreviations: TPI, Triosephosphate Isomerase; TPI Df, Triosephosphate Isomerase Deficiency; WT, Wild-type; G3P, Glyceraldehyde-3-phosphate; DHAP, Dihydroxyacetone phosphate; Hsp70, Heat shock protein 70; Hsp90, Heat shock protein 90; RNAi, RNA interference; UTR, Untranslated Region; MCV, Mean Corpuscular Volume; Hgb, Hemoglobin; Hct, Hematocrit.

* Corresponding author. Department of Pharmacology and Chemical Biology, University of Pittsburgh, Pittsburgh, PA, USA.
E-mail address: mjp44@pitt.edu (M.J. Palladino).

https://doi.org/10.1016/j.crneur.2022.100062
Received 13 May 2022; Received in revised form 30 September 2022; Accepted 30 October 2022
Available online 9 November 2022

(*TPI1*^{E105D}; previously known clinically as *TPI1*^{E104D}), while heterozygous family members are asymptomatic (Orosz et al., 2009; Shi et al., 2005). However, multiple alternative disease-causing mutations have been identified such as *TPI1*^{I171V}, *TPI1*^{R190Q}, *TPI1*^{Q181P} and *TPI1*^{F241L} (Arya et al., 1997; Hollan et al., 1993; Orosz et al., 2009; Roland et al., 2019; VanDemark et al., 2022). Importantly, many of these alleles only seem to be pathogenic when present as a compound heterozygote with *TPI1*^{E105D}, illustrating the pathogenic nature of this mutation. The *TPI1*^{E105D} mutation is thought to cause degradation of functional TPI protein, leading to symptomologies of the disease similar to the *TPI*^{sgk} mutation in *Drosophila melanogaster* (Cabrera et al., 2018; De La Mora-De La Mora et al., 2013; Rodriguez-Almazan et al., 2008; Seigle et al., 2008; Vogt et al., 2021). It has been demonstrated that *TPI*^{sgk} in *Drosophila* is targeted for degradation by the proteasome, through the activities of molecular chaperones such as Hsp70 and Hsp90 (Hrizo and Palladino, 2010). Other potential regulators of mutant TPI protein have been identified through an RNAi screen in *Drosophila*, however, the mechanism behind their action needs further investigation (Hrizo et al., 2021). Additionally, altered dimerization of TPI^{E105D} protein may affect stability of the protein and play a role in the pathogenesis of TPI Df (Ralser et al., 2006; Rodriguez-Almazan et al., 2008).

Much of the reported TPI Df research has been completed in invertebrate models of the disease, such as *Drosophila,* or cellular models. While glycolytic enzymes are highly conserved, there are several limitations to using an invertebrate or *in vitro* model to study this human disease such as the lack of red blood cells, differences in neuromuscular physiology and organ systems (e.g. liver and spleen), and a less complex nervous system. A vertebrate model of TPI Df would be more clinically relevant and enable efficacy testing. In particular, the use of a murine model allows for a more relevant physiology to human disease in an organism which is already well-studied and is relatively easy to genetically manipulate. Other lab groups have isolated mutations in mouse *Tpi1*, however, none of these studies were focused on modeling TPI Df and, thus, did not create the *Tpi1*^{E105D} mutation (Conway et al., 2018; Pretsch, 2009; Segal et al., 2019). The currently available mouse *Tpi1* mutant strains have been informative and model hemolytic anemia, however, they lack key symptoms of human TPI Df, such as neuromuscular dysfunction. In support of the protein-stability hypothesis, mouse models with markedly reduced TPI catalytic activity do not exhibit neuromuscular disease akin to TPI Df (Pretsch, 2009; Segal et al., 2019).

Here we report the production of a novel murine model of TPI Df which recapitulates the full scope of human disease symptoms. The CRISPR-Cas9 system was utilized to generate a murine model of TPI Df, *Tpi1*$^{E105D/null}$. This mutation combination is akin to human patients carrying a *TPI1*^{E105D} allele paired with *TPI1*^{R190Q}, a strong hypomorphic loss of function allele, a combination that results in an accelerated and severe disease course (Roland et al., 2019). Two parent CRISPR strains were generated, one with a *Tpi1*^{E105D} missense mutation as well as a silent mutation, and one with a heterozygous 11 base-pair deletion in the *Tpi1* gene which creates a knockout of *Tpi1* (*Tpi1*^{null}). We have also established a control mouse line with only the silent mutation to be used in future studies as an ideal genetic control for these engineered genotypes. Compound heterozygous *Tpi1*$^{E105D/null}$ offspring demonstrate characteristic symptoms of severe human TPI Df. The phenotype of these animals includes altered posture, hindlimb weakness, decreased body weight, strained breathing, hemolytic anemia, irregular movements that resemble myoclonic jerks, and a severely reduced longevity. These animals also show evidence of marked spleen pathology. *Tpi1*$^{E105D/E105D}$ mice are homozygous viable, similar to the human mutation, and exhibit phenotypes similar to *Tpi1*$^{E105D/null}$ animals but are less severe. These *Tpi1*$^{E105D/E105D}$ animals have not been characterized in detail as the animals live significantly longer and the phenotypes develop more slowly (data not shown). Future studies will be needed to fully characterize *Tpi1*$^{E105D/E105D}$ animals.

2. Materials and methods

2.1. CRISPR generation of TPI Df mice

A gRNA binding site near the targeted *Tpi1*^{E105D} knock-in (KI) mutation site (see Fig. 1A) was identified using Deskgen Guide Picker (Hough et al., 2016). This gRNA target site was used to produce an Alt-R CRISPR-Cas9 crRNA (Integrated DNA Technologies, Coralville, IA) which was hybridized to a universal 67-mer Alt-R CRISPR-Cas9 tracrRNA (IDT) to produce a gRNA. A 101 nucleotide PAGE-purified Ultramer single stranded DNA Oligonucleotide (IDT) with three phosphorothioate modifications (Renaud et al., 2016) on each end was synthesized that was homologous to the target locus and harbored the desired A to C knock-in mutation and a T to C silent mutation (see Fig. 1A) and was used as a repair template. The silent mutation was included to prevent gRNA binding to the mutated locus. Single cell C57BL/6J embryos were electroporated with gRNA (200 ng/μl), IDT Alt-R® HiFi Cas9 Nuclease V3 protein (50 ng/μl), and repair template (200 ng/μl) using a Bio-Rad Gene Pulser Xcell electroporator and 1 mm-gap slide electrode with the following electroporation parameters: 25V pulse x 5; 3msec pulse time; 100msec pulse interval. Following electroporation, surviving embryos were transferred to the oviducts of CD1 (Charles River) psuedopregnant recipient females. Guide RNA off target sites were predicted and ranked using CRISPOR (Concordet and Haeussler, 2018). The top 17 sites (Table S1) based on CFD score were amplified from founder mouse DNA and Sanger sequenced.

2.2. Animal care

All animals were maintained at the University of Pittsburgh with oversight from the Institutional Animal Care and Use Committee (IACUC) and in accordance with the Guide for the Care and Use of Laboratory Animals published by the U.S. National Institutes of Health (National Research Council, 2011). Animals were housed in individually ventilated cages under specific pathogen free conditions with 12h light/dark cycles (lights on at 7:00AM and off at 7:00PM) and had free access to food and water. Mutant mice with particularly severe muscular phenotypes were supplied moistened food on the bottom of the cage for ease of access. A humane endpoint was used to determine conditions for sacrifice. This endpoint was either losing 20% of body weight over the span of a week, or the loss of righting reflex. Animals were euthanized via CO_2 inhalation or isoflurane overdose. Genotyping was conducted at ~2 weeks of age from tail-snip DNA that was isolated with Lucigen QuickExtract DNA Extraction Solution (Lucigen, Middleton, WI) and amplified using Platinum™ Taq DNA Polymerase High Fidelity (Invitrogen, Cat. No: 11304011). Primers used for genotyping were 5′-TCAGGTGAGATGGAGGCAGA-3' (forward) and 5′-TGCTCGAACACGACCTTCTC-3' (reverse). Amplified DNA was sent to Genewiz (Azenta Life Sciences, South Plainfield, NJ) for Sanger sequencing, and was analyzed using SnapGene (GSL Biotech LLC, Chicago, IL) to determine genotypes (Fig. S1).

2.3. Tissue collection

Upon reaching conditions for humane sacrifice, phenotypic animals and their control littermates were sacrificed simultaneously for investigation using isoflurane overdose. Terminal weights for animals were recorded before being dissected. To start the dissection, a T-shaped incision was made across the abdomen. The diaphragm was excised to gain access to the heart, and a cardiac puncture was performed on the left ventricle with a 1 inch 23-gauge needle (BD, Cat no. 309588). Whole blood samples were stored within EDTA-coated tubes at 4 °C until being shipped to IDEXX BioAnalytics (Westbrook, ME) for analysis. Next, the liver was dissected out of the animal and cut into three equal parts. Liver samples were flash frozen in liquid nitrogen and stored at −80 °C until lysis and subsequent Western blot analysis. Spleen tissues were dissected

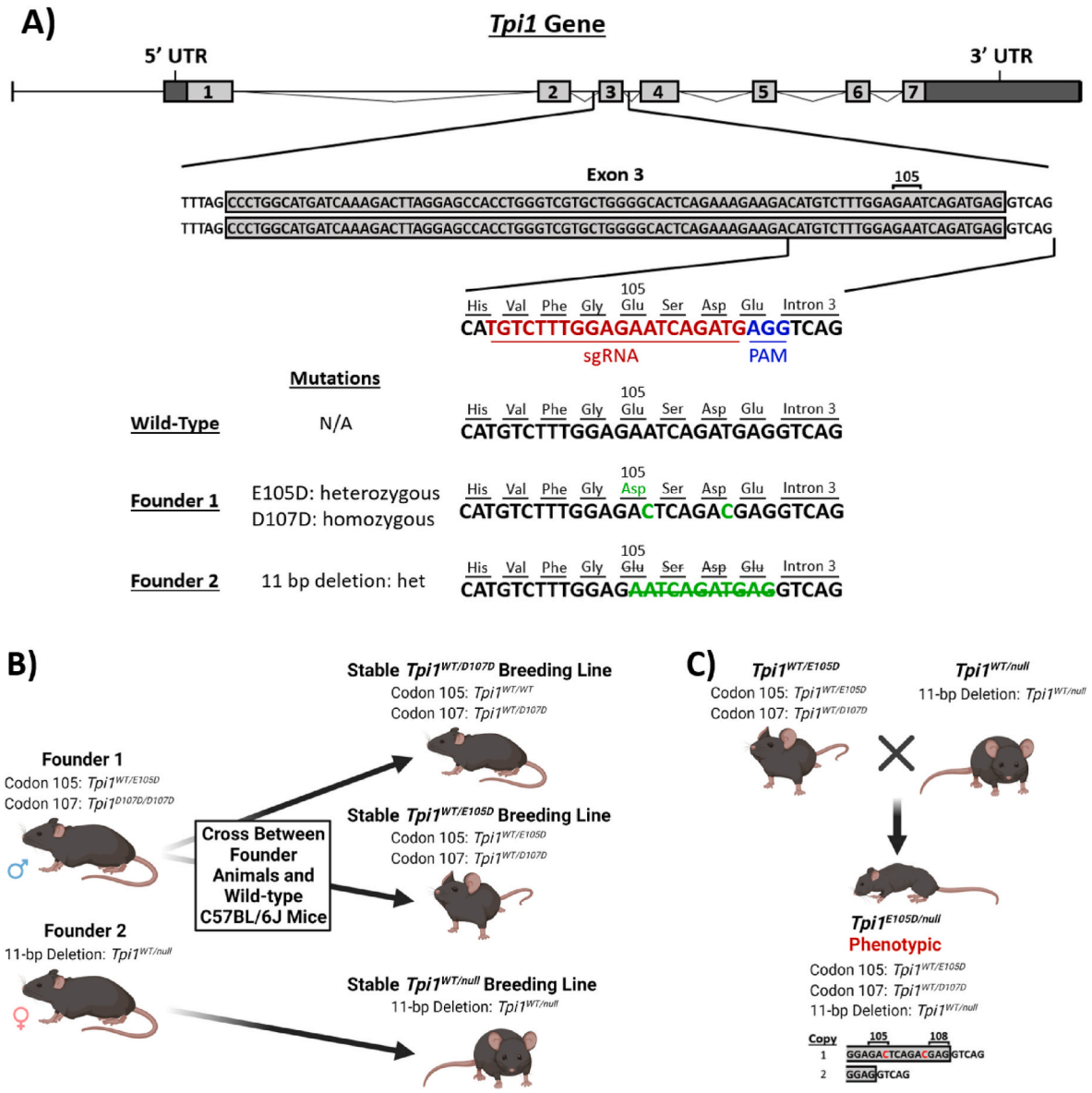

Fig. 1. CRISPR generation and creation of stable breeding lines. A) Map of murine *Tpi1* gene with magnification of the CRISPR modification region. The sgRNA binding site is shown in red and protospacer adjacent motif (PAM) is shown in blue. Sequences for WT animals and both founder animals are shown, with mutation sites marked in green text. The 11 base pair deletion is marked by green strike-through text. Founder 1 has a heterozygous A → C substitution at the 105th codon, changing the coded amino acid from a glutamate to an aspartate. Additionally, founder 1 harbors a homozygous T → C substitution at the 107th codon, which does not change the encoded amino acid. Founder 2 has an 11 base pair deletion starting at the second base pair in codon 105. Note: this deletion will result in a frameshift, leading to a knockout of the *Tpi1* gene. B) Diagram showing the formation of three stable breeding lines from the 2 founder animals. C) Breeding scheme for generation of $Tpi1^{E105D/null}$ animals. The bottom of the panel visualizes the inherited copies of *Tpi1* from both parents in $Tpi1^{E105D/null}$ animals. Panels B and C were created with BioRender.com. (For interpretation of the references to colour in this figure legend, the reader is referred to the Web version of this article.)

and weighed after trimming of visceral fat. The spleen was then cut into 4 equal pieces lengthwise. The two middle pieces of spleen tissue were placed in either 4% paraformaldehyde (PFA) or 10% buffered formalin (Sigma-Aldrich, Cat no. HT501128) and were fixed overnight at either 4 °C (PFA) or room temperature (formalin). After fixation, spleen tissue was stored in 70% ethanol at 4 °C. Finally, brain tissue was collected and sectioned into two hemispheres. Brain samples were then flash frozen in liquid nitrogen and stored at −80 °C until lysis and Western blot analysis.

2.4. Bloodwork analysis

Blood samples were shipped to the IDEXX BioAnalytics location in North Grafton, MA, overnight in Styrofoam coolers containing 4 °C cold packs. Upon receipt at IDEXX BioAnalytics, the EDTA-anticoagulated whole-blood samples were examined microscopically to assess sample quality, which was noted on the analysis reports. Samples were subjected to either a blood count panel or a comprehensive blood count with reticulocyte hemoglobin. The blood count panel included analysis of white and red blood cell count (WBC and RBC), hemoglobin (Hgb), hematocrit (Hct), mean corpuscular volume (MCV), mean corpuscular hemoglobin (MCH), and mean corpuscular hemoglobin concentration (MCHC). The comprehensive blood count with reticulocyte hemoglobin contains all of the tests from the blood count panel but also includes platelet counts, reticulocyte counts, reticulocyte hemoglobin, a leukocyte differential, and morphological analysis. Blood samples were analyzed through use of the flow-cytometry-based Sysmex XT-2000iV Automated Hematology Analyzer (Sysmex, Kobe, Hyogo, Japan).

Differentiation of leukocytes was based on species-specific gates that were previously validated. A blood smear was microscopically investigated to assess morphological abnormalities and to confirm leukocyte differential counts. All blood samples were analyzed within 5 days of collection. If blood samples exhibited clotting or if any other issues were reported from IDEXX, the sample was not used in the analysis, and data was collected from another animal of the same genotype/sex to fill in this gap. In total, 6 initial blood samples were not included in the analysis (with no more than 2 such samples in a single genotype): 3 due to sample quality issues and 3 due to a sample volume that was insufficient for analysis.

2.5. Western blot

Flash frozen tissues were lysed in 800 μL of RIPA buffer (Thermo Scientific, Cat no. 89900) using an IKA Ultra-Turrax T8 mechanical homogenizer (IKA, Staufen, Germany). Samples were then centrifuged at 12,000×*g* for 20 min, and supernatant was collected. Protein concentrations in the lysate were calculated via a BCA assay (Thermo Scientific, Cat no. 23225). Lysates were loaded into 12% acrylamide gels with 35 μg of total protein per well. The gel was then run in a BioRad running tank for 50 min at 200V in 1x SDS-PAGE running buffer (Fisher BioReagents, Cat no. BP13414). Proteins were transferred onto a 0.45 μm PVDF membrane (Thermo Scientific, Cat no. 88518) using a semi-dry transfer tank (BioRad, Hercules, CA) for 3 h at 12V. After transfer, blots were blocked in LiCor Intercept Protein-Free Blocking Buffer (LiCor, Cat no. 927–80001) for 2 h. Primary antibodies for rabbit anti-TPI (Santa Cruz Biotechnology sc-30145, 1:5000), mouse anti-β-tubulin (Santa Cruz Biotechnology sc-365791, 1:1000), or mouse anti-β-actin (mAbcam 8226, 1:1000) were added onto the blot in blocking buffer and were incubated overnight at 4 °C. Blots were washed six times for 5 min each in PBS-T (1x PBS with 0.05% Tween 20). Secondary antibodies for goat anti-mouse 680 (Invitrogen A-21057, 1:20,000) and donkey anti-rabbit 800 (LiCor 926–32213, 1:20,000) were added to LiCor Intercept Protein-Free Blocking Buffer with 0.1% Tween 20. Blots were incubated in secondary antibodies for 2 h at room temperature in the dark. Blots were then washed six times for 5 min each in PBS-T. The LiCor Odyssey cLx and Image Studio version 5.2 (LiCor, Lincoln, NE) were used to visualize and analyze western blots.

2.6. Imaging

Tissues that were fixed in either 4% PFA or 10% buffered formalin were sent to the Pitt Biospecimen Core (University of Pittsburgh, Pittsburgh, PA) for processing, embedding, sectioning, and staining. Tissues were embedded in paraffin and sectioned at a thickness of 5 μm. Sections were placed on microscope slides and stained with hematoxylin and eosin. Images were taken using an Olympus BX51 fluorescence microscope (Olympus, Tokyo, Japan) with 20x total magnification. Analysis was completed using FIJI (C. A. Schneider et al., 2012). The cross-sectional area of spleen sections was calculated using the magic wand tool at threshold of 100. The area of white pulp was calculated by manually outlining the white pulp regions that are stained in purple by hematoxylin and eosin staining and recording the area of the outlined white pulp. The white pulp area was then expressed as a percentage of total cross-sectional area.

2.7. Statistics

All statistical tests were performed using GraphPad Prism 9 Software (San Diego, CA). Normality of data was assessed before all statistical analyses by visualizing a QQ-plot. All data collected followed a normal distribution. Bartlett's test was used to determine whether the groups to be compared had equal standard deviations. Comparisons where all groups had equal variances were made using one-way ANOVA. Comparisons where groups had unequal variances were made using a Welch's ANOVA. Post-hoc comparisons were made using Tukey's multiple comparisons test after ordinary one-way ANOVA or Dunnett's multiple comparisons test after a Welch's ANOVA. Survival curves were compared using a log-rank test. Categorical data, such as breeding outcomes, were compared using a chi-square goodness-of-fit test. All data were evaluated for sex differences using a two-way ANOVA, and any data which demonstrated a significant effect of sex were analyzed separately. Data which showed no evidence of a sex difference were pooled.

3. Results

3.1. Generation of *Tpi1*$^{WT/E105D}$ and *Tpi1*$^{WT/null}$ mice

Mutations in the *Tpi1* gene were engineered using CRISPR and two founder animals resulting from this manipulation were selected to establish two mouse lines (Fig. 1A). Founder animal 1 was a male that harbored a heterozygous *Tpi1*$^{WT/E105D}$ mutation as well as a homozygous silent mutation which does not change the amino acid sequence (*Tpi1*$^{D107D/D107D}$). This silent mutation was included to prevent gRNA binding to the knock-in locus, and it can be used as a control for the knock-in chromosome. Founder animal 2 was a female and was modified to have a heterozygous 11 base pair deletion beginning at the 2nd nucleotide in the 105th codon, creating a frameshift and knock-out of *Tpi1* (*Tpi1*$^{WT/null}$). Both founder animals were confirmed to have no off-target CRISPR modifications in any of the 17 most highly ranked potential off-target sites examined (Supplementary Table S1).

Founder animals were mated with parental wild type C57BL/6J mice to create three stable breeding lines (Fig. 1B). Briefly, founder 1 was mated with multiple WT C57BL/6J female mice. This founder transmitted both the *Tpi1*^{E105D} and *Tpi1*^{D107D} mutations to 62% of F1 offspring. These offspring were used to create a stable *Tpi1*$^{WT/E105D;D107D}$ breeding line. The remaining 38% of F1 offspring inherited the silent *Tpi1*^{D107D} mutation only. These offspring were used to create a stable *Tpi1*$^{WT/D107D}$ breeding strain bearing only the control silent mutation. For clarity, the *Tpi1*$^{E105D;D107D}$ chromosome will be referred to as *Tpi1*^{E105D}. Founder 2 was mated with a male WT C57BL/6J mouse, and offspring which inherited the 11 base pair deletion were used to create a stable *Tpi1*$^{WT/null}$ breeding strain. To obtain mice modeling severe TPI Df, the *Tpi1*$^{WT/E105D}$ strain was mated with the *Tpi1*$^{WT/null}$ strain to generate *Tpi1*$^{E105D/null}$ animals (Fig. 1C). All breeding pair combinations resulted in normal litter sizes when counted on the day of birth (Fig. 2A). Genotyping was conducted on tail snip DNA collected at post-natal day 14 (Supplementary Fig. S1). Litters produced by *Tpi1*$^{WT/null}$ x *Tpi1*$^{WT/null}$ breeding pairs never produced *Tpi1*$^{null/null}$ pups and Mendelian inheritance ratios were altered as predicted for a lethal mutation (Fig. 2B). Importantly, pups that were born survived to the weaning age in *Tpi1*$^{WT/null}$ x *Tpi1*$^{WT/null}$ litters, which confirms that *Tpi1*$^{null/null}$ animals are never born. These data indicate the essential nature of the *Tpi1* gene and the inviable nature of *Tpi1*$^{null/null}$ animals.

3.2. Protein levels in *Tpi1*$^{E105D/null}$ mice

TPI protein levels were evaluated in *Tpi1*$^{E105D/null}$ animals and their littermate controls. In the brain, TPI levels were reduced in a genotype-dependent stepwise fashion where *Tpi1*$^{WT/WT}$ animals have the most TPI, *Tpi1*$^{WT/E105D}$ animals have an ~30% reduction in TPI levels, *Tpi1*$^{WT/null}$ animals have an ~40% decrease in TPI levels, and *Tpi1*$^{E105D/null}$ animals have an ~95% reduction in TPI levels (Fig. 3, A and C). In liver, a similar pattern was identified, where *Tpi1*$^{WT/WT}$ animals have the most TPI, *Tpi1*$^{WT/E105D}$ animals have an ~35% reduction in TPI levels, *Tpi1*$^{WT/null}$ animals have an ~50% reduction in TPI levels, and *Tpi1*$^{E105D/null}$ animals have an ~95% reduction in TPI levels (Fig. 3, B and D). These data are consistent with the *Tpi1*^{E105D} mutation encoding a protein with very low stability, as has been observed in patient samples bearing the same mutation (Hrizo et al., 2021). Western blots from

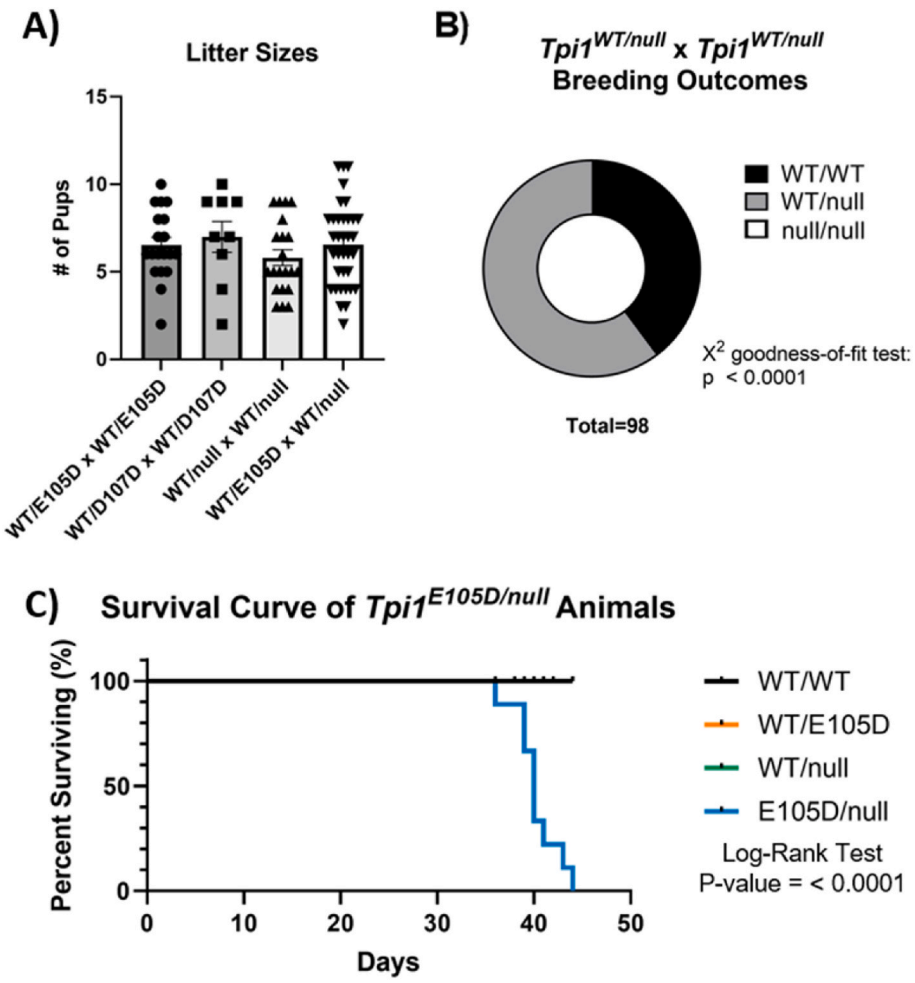

Fig. 2. Breeding and longevity of TPI Df animals. A) Litter sizes of different breeding combinations. Expressed as mean ± SEM. For the number of litters used in litter size comparison, N = 9–35 litters per breeding genotype combination. A one-way ANOVA was not significant. B) Genotype outcomes of $Tpi1^{WT/null}$ x $Tpi1^{WT/null}$ breeding pairs, demonstrating the inviable nature of $Tpi1^{null/null}$ animals. C) Survival curve of $Tpi1^{WT/WT}$, $Tpi1^{WT/E105D}$, $Tpi1^{WT/null}$ and $Tpi1^{E105D/null}$ animals. In survival curve, N = 9–10 animals per group. Note: $Tpi1^{WT/E105D}$, $Tpi1^{WT/null}$ are indistinguishable from $Tpi1^{WT/WT}$.

$Tpi1^{E105D/E105D}$ animal tissues demonstrate a reduction compared to $Tpi1^{WT/WT}$ and $Tpi1^{WT/E105D}$ animal tissues that is less severe than $Tpi1^{E105D/null}$ animals (Supplemental Fig. S2). The protein levels in both liver and brain tissues of $Tpi1^{E105D/E105D}$ animals are intermediate to that from $Tpi1^{WT/E105D}$ and $Tpi1^{E105D/null}$ animal tissues, corresponding with their less-severe disease course.

3.3. $Tpi1^{E105D/null}$ mice as a model of severe TPI Df

The core symptoms of human TPI Df include anemia, progressive neuromuscular dysfunction, postural abnormalities, and severely reduced longevity. $Tpi1^{E105D/null}$ animals were found to have a marked reduction in longevity when compared to their littermate counterparts (Fig. 2C). Locomotor phenotypes became evident ~30 days of age in $Tpi1^{E105D/null}$ animals that progressively worsened. This phenotype began with an altered gait and then progressed to general hindlimb weakness as evidenced by reduced hindlimb splaying (Fig. 4B) and dragging of the hindlimbs. At ~35 days of age, $Tpi1^{E105D/null}$ animals experienced difficulty breathing and also jerky movements that resembled myoclonic jerks (Supplementary Video 1). Towards the end-stage of $Tpi1^{E105D/null}$ animals, prominent emaciation (Fig. 4A) and a hunched posture were evident (Fig. 4C). Importantly, symptomatic animals were supplied softened food on their cage floor, so this phenotype is not simply due to animals not being able to reach food. These phenotypes were never visible in $Tpi1^{WT/WT}$, $Tpi1^{WT/E105D}$, or $Tpi1^{WT/null}$ animals (Fig. 4 and data not shown). Additionally, difficult breathing and abrupt motions resembling myoclonic jerks were noted in $Tpi1^{E105D/null}$ animals (Supplementary Video 1) – these phenotypes were not observed in any wild-type animals or animals carrying a wild-type allele paired with a mutant allele. The body weight of $Tpi1^{E105D/null}$ animals of both sexes were significantly reduced compared to age and sex matched $Tpi1^{WT/WT}$, $Tpi1^{WT/E105D}$, and $Tpi1^{WT/null}$ animals (Fig. 5A and B). Importantly, $Tpi1^{WT/E105D}$ and $Tpi1^{WT/null}$ animals did not differ in weight from $Tpi1^{WT/WT}$ animals (Fig. 5A and B).

Supplementary video related to this article can be found at https://doi.org/10.1016/j.crneur.2022.100062

3.4. Hemolytic anemia in $Tpi1^{E105D/null}$ mice

In humans, anemia is a known result of TPI Df and is often an early symptom of the disease (Schneider et al., 1965). $Tpi1^{E105D/null}$ animals were found to have reduced hemoglobin (Fig. 5C) and hematocrit levels (Fig. 5D) at humane sacrifice (~40 days of age) when compared to age-matched $Tpi1^{WT/WT}$, $Tpi1^{WT/E105D}$, and $Tpi1^{WT/null}$ animals. The MCV was found to be increased in $Tpi1^{E105D/null}$ animals when compared to $Tpi1^{WT/WT}$, $Tpi1^{WT/E105D}$, and $Tpi1^{WT/null}$ animals (Fig. 5E). Finally, $Tpi1^{E105D/null}$ animals also displayed a markedly increased reticulocyte count (Fig. 5F). As with body weight, the hematology examined did not differ between $Tpi1^{WT/WT}$, $Tpi1^{WT/E105D}$, and $Tpi1^{WT/null}$ animals.

3.5. Spleen pathology in $Tpi1^{E105D/null}$ mice

Spleen enlargement was noted in all $Tpi1^{E105D/null}$ mice. Spleens were examined by histopathological hematoxylin and eosin staining of cross-sectioned organs (Fig. 6A and B). Images of $Tpi1^{E105D/null}$ spleens show extensive red blood cell pooling and a marked reduction of the white

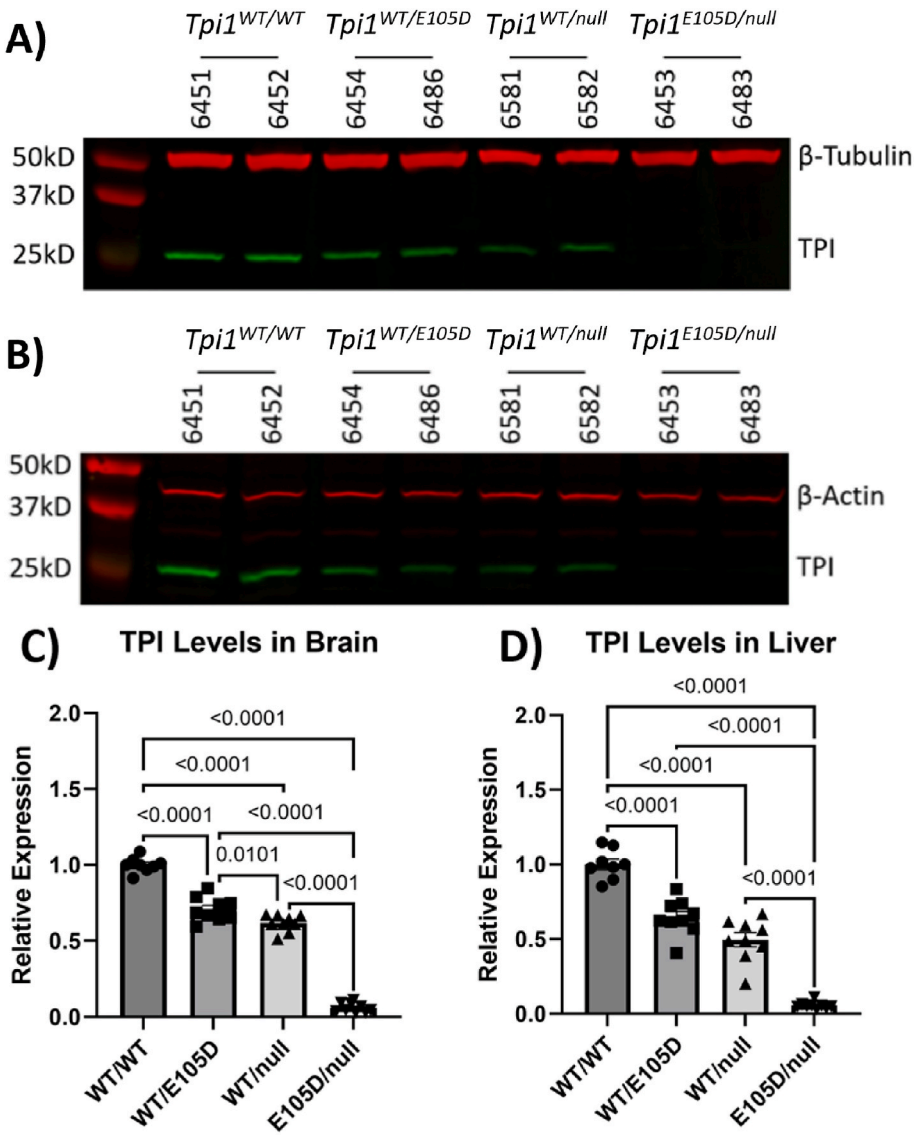

Fig. 3. Western blot analysis of TPI levels. Panels A and B show representative western blots of brain and liver tissue, respectively. Panels C and D are quantifications of TPI levels from Western blot analyses. Expressed as mean ± SEM. N = 8–9 animals per group.

pulp area. Male and female spleen weights were found to be significantly increased in $Tpi1^{E105D/null}$ animals when compared to $Tpi1^{WT/WT}$, $Tpi1^{WT/E105D}$, and $Tpi1^{WT/null}$ animals (Fig. 6C). $Tpi1^{E105D/null}$ animals have a reduced body weight (Fig. 5A and B); thus, the spleen weight was expressed as a percentage of total body weight. The percent of total body weight of the spleen in both male and female $Tpi1^{E105D/null}$ animals was found to be significantly increased when compared to $Tpi1^{WT/WT}$, $Tpi1^{WT/E105D}$, and $Tpi1^{WT/null}$ animals (Fig. 6D). Images of spleen tissue were analyzed for both the total cross-sectional area and the area occupied by the white pulp of the spleen. The cross-sectional area of spleen tissue was found to be significantly increased in $Tpi1^{E105D/null}$ animals when compared to $Tpi1^{WT/WT}$ animals (Fig. 6E). White pulp area, expressed as a percentage of total cross-sectional area, was found to be significantly decreased in $Tpi1^{E105D/null}$ animals from both sexes when compared to $Tpi1^{WT/WT}$, $Tpi1^{WT/E105D}$, and $Tpi1^{WT/null}$ animals (Fig. 6F and G).

4. Discussion

TPI Df is a devastating childhood disease in dire need of treatment options. Currently, patients with a TPI Df diagnosis are provided extremely limited treatment options consisting of dietary changes and supplementation, neither of which has any evidence of improved lifespan or quality of life. Many patients also receive supportive care in the form of feeding tubes and respirators, which may extend the longevity but do not restore quality of life. To develop more effective treatment options for these patients, more research must be done to better understand disease pathogenesis in TPI Df. Hitherto, TPI Df research has relied largely on invertebrate models of disease or *in vitro* cellular models. While these studies have been informative regarding the pathogenesis of the disease, it is possible these models lack clinical relevance and are certainly poorly suited for testing novel therapies. Thus, a mouse model of TPI Df that captures key features of this multisystemic disease is imperative to advance the field. Three other groups have produced murine models which do mimic limited aspects of the human disease, however, the full scope of TPI Df symptoms was not realized (Conway et al., 2018; Pretsch, 2009; Segal et al., 2019). Importantly, all three previously generated murine models lack neuromuscular dysfunction, a key symptom of human disease. Interestingly, Conway et al. demonstrated significantly decreased TPI protein levels in bone marrow lysates from their $Tpi1^{F57S}$ model ($Tpi1^{F7S}$ using our numbering; Conway et al., 2018). Although protein levels reported in the $Tpi1^{F7S}$ murine model

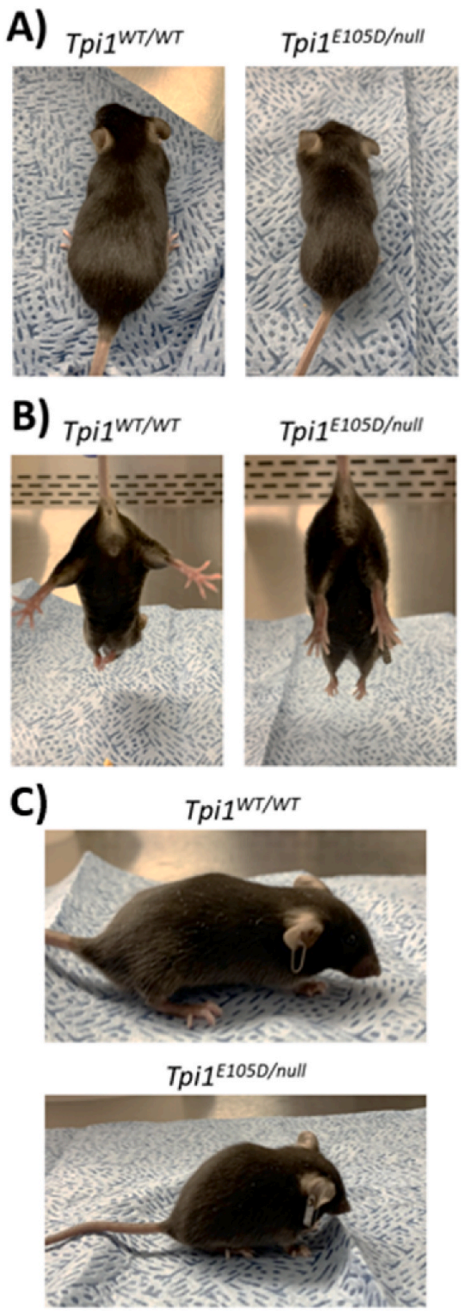

Fig. 4. Postural phenotype of *Tpi1*$^{E105D/null}$ animals. A) Healthy mouse pictured on left, *Tpi1*$^{E105D/null}$ mouse with prominent emaciation on the right. B) Typical hindlimb splaying behavior on the left, *Tpi1*$^{E105D/null}$ mouse with strongly reduced hindlimb splaying. C) Postural abnormality of *Tpi1*$^{E105D/null}$ animal with prominent kyphosis in the bottom panel, with typical posture demonstrated in the top panel.

were reduced, they did not observe neuromuscular phenotypes akin to TPI Df (Conway et al., 2018). These differences could be due to any number of reasons most notably the extent of *Tpi1* reduction, mutation specific effects on function, or the use of different background strains (C57BL/6J vs. SJL). This work details a newly generated murine model of TPI Df which recapitulates key hallmarks of the human disease such as signs of neuromuscular dysfunction, hemolytic anemia, and a markedly reduced longevity.

The most common mutation resulting in human TPI Df is the *TPI1*^{E105D} mutation (Orosz et al., 2006). The sequence of *TPI1* is highly conserved among organisms due to the integral role in glycolysis of its encoded protein, allowing us to model this same mutation within the mouse genome. This work utilized CRISPR to introduce this mutation into the murine *Tpi1* gene. Both *Tpi1*$^{E105D/E105D}$ and *Tpi1*$^{E105D/null}$ animals show phenotypes similar to the human disease, with the latter genotype being akin to severe TPI Df disease. *Tpi1*$^{E105D/null}$ mice do not survive to breeding age which is consistent with the severe childhood disease seen in human TPI Df patients. The markedly reduced lifespan of *Tpi1*$^{E105D/null}$ animals and rapid onset of severe phenotypes makes them an attractive model for the study of TPI Df and allow for easily testable outcome measures for potential therapeutic interventions within a short time frame, e.g., longevity, anemia, protein levels, and behavioral analyses. While *Tpi1*$^{E105D/E105D}$ animals show clear phenotypes similar to the human disease, these animals have a less severe course of disease that progresses in a similar manner to *Tpi1*$^{E105D/null}$ animals, however this phenotype appears later in the lifespan (around 50 days of age) and progresses more slowly. Due to the later onset and slower progression of *Tpi1*$^{E105D/E105D}$ animals, their full characterization is beyond the scope of this manuscript.

Tpi1$^{E105D/null}$ mice recapitulate key aspects of the human disease. They have a greatly reduced longevity, with death occurring between 36 and 44 days of age. *Tpi1*$^{E105D/null}$ animals show a near 95% reduction in TPI levels compared to *Tpi1*$^{WT/WT}$ animals in both brain and liver, indicating the *Tpi1*^{E105D} protein likely has reduced stability, as has been reported previously (Rodriguez-Almazan et al., 2008; Vogt et al., 2021). This reduction in TPI levels leads to many characteristic TPI Df symptoms. *Tpi1*$^{E105D/null}$ animals have markedly altered posture and size compared to their littermates. They present with decreased body weight, a hunched back, weakened hindlimbs which display reduced splaying behavior when suspended by the tail, and a noticeably emaciated appearance. Additionally, these animals showed pronounced disordered breathing and prominent movements which resemble myoclonic jerks. While some of these postural phenotypes could be exacerbated by the moribund condition of the mice, the progression of symptoms is consistent with marked neuromuscular dysfunction. Importantly, the first phenotypes to become apparent are altered gait, strained breathing, reduced hindlimb splaying, and dragging of the hindlimbs all consistent with neuromuscular impairment. The precise origin of the neuromuscular dysfunction is not clear at this time and will be the subject of future studies. *Tpi1*$^{E105D/null}$ animals also have hemolytic anemia, as indicated by low hemoglobin levels, low hematocrit levels, and an elevated reticulocyte count. They display an increased MCV, indicating a macrocytic hemolytic anemia similar to what is seen in human TPI Df (Conway et al., 2018). In addition to the presence of hemolytic anemia, extensive spleen pathology is also noted. *Tpi1*$^{E105D/null}$ animals display a significant increase in spleen weight, which is even more drastic when spleen weight is expressed as a percentage of total body weight. The cross-sectional area of the spleen is enlarged in *Tpi1*$^{E105D/null}$ animals when compared to littermate controls, and white splenic pulp is markedly reduced. This loss of white splenic pulp may help explain human TPI Df patients' susceptibility to infection. There is also significant disruption of the spleen anatomy by destroyed red blood cells, indicative of the spleen's role in hemolytic anemia. Splenic destruction of red blood cells is consistent with red blood cells lacking mitochondria and being reliant upon glycolysis for energy production. While we measured the white pulp area in the spleen, our method relied solely upon visual inspection of H&E-stained spleen tissue, which is a limitation. Follow-up studies should examine Ter119 IHC staining of the spleen to evaluate the proportion of erythroid lineage.

Together, these data suggest that *Tpi1*$^{E105D/null}$ mice are an excellent model of TPI Df. To our knowledge, this is the first model that is capable of recapitulating numerous key aspects of human disease. The development of a murine model of TPI Df is necessary to advance the field of study. This model will allow for detailed mechanistic studies of TPI Df, including investigation of neuropathology and myopathology within the context of a mammalian system. Important follow-up experiments that should occur in this model are tissue specific bioenergetic studies,

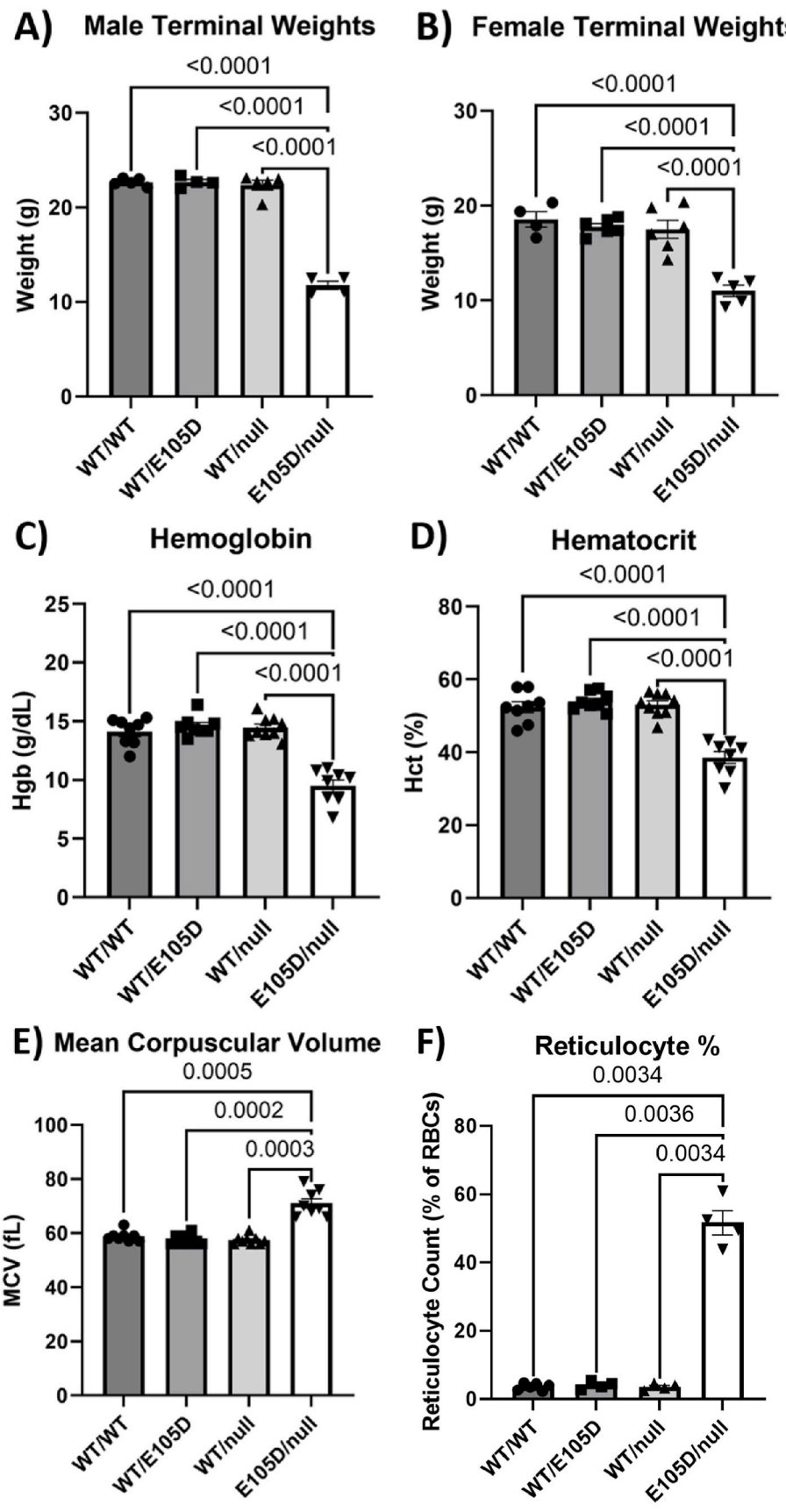

Fig. 5. Hematology and terminal weights of TPI Df animals. A) Male terminal weights of *Tpi1*$^{E105D/null}$ animals and littermates, N = 4–5 animals per group. B) Female terminal weights of *Tpi1*$^{E105D/null}$ animals and littermates, N = 4–6 animals per group. Panels C, D, and E represent hemoglobin, hematocrit, and mean corpuscular volume values, respectively. N = 8–9 animals per group. F) Reticulocyte count expressed as a percentage of total red blood cells. N = 4–6 animals per group. All are expressed as mean ± SEM.

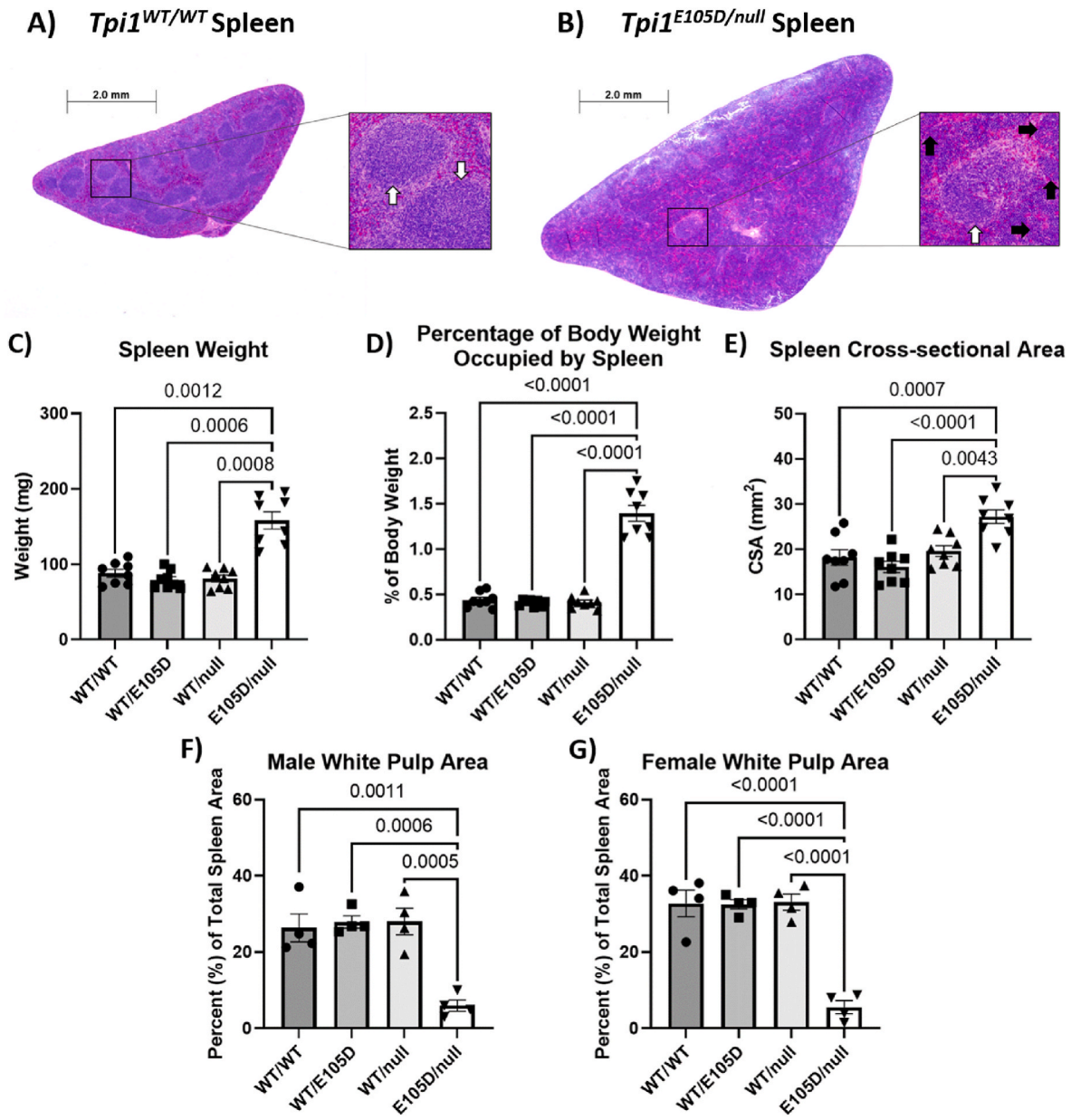

Fig. 6. Spleen pathology in TPI Df mice. Panels A and B show representative images of cross-sectioned spleen tissue from *Tpi1*$^{WT/WT}$ (A) and *Tpi1*$^{E105D/null}$ (B) animals. White arrows demarcate white splenic pulp, black arrows demarcate red blood cell pooling in the red pulp. C) Spleen weights pooled from male and female animals. D) Spleen weight expressed as a percentage of total body weight pooled for both male and female animals. E) Cross-sectional area of spleens pooled from male and female *Tpi1*$^{E105D/null}$ animals and littermate controls. F) and G) White pulp area of spleens from male *Tpi1*$^{E105D/null}$ animals (F) and female animals (G) compared to littermate controls. All are expressed as mean ± SEM. N = 4 animals per group per sex. Panels C, D and E have males and females pooled due to lack of sex differences, for a total of 8 animals per group. (For interpretation of the references to colour in this figure legend, the reader is referred to the Web version of this article.)

investigation of biochemical and structural changes in the neuromuscular system, and evaluation of neuropathology. These studies will undoubtedly lead to a better understanding of the pathological changes which occur in disease. The *Tpi1*$^{E105D/null}$ model will also allow for the evaluation of novel therapeutics for the treatment of TPI Df within a more clinically relevant organism (Vogt et al., 2021). Future work with this model will allow for discoveries in the field of TPI deficiency that will lead to better treatment outcomes, and a better prognosis for TPI Df patients.

CRediT authorship contribution statement

Tracey D. Myers: Investigation, Formal analysis, Writing – review & editing, Final Approval. **Carolyn Ferguson:** Investigation, Writing – review & editing, Final Approval. **Eric Gliniak:** Investigation, Writing – review & editing, Final Approval. **Gregg E. Homanics:** Conceptualization, Methodology, Investigation, Writing – review & editing, Final Approval. **Michael J. Palladino:** Conceptualization, Methodology, Funding acquisition, Writing, Writing – review & editing, Final Approval.

Declaration of competing interest

The authors declare that they have no known competing financial interests or personal relationships that could have appeared to influence the work reported in this paper.

Data availability

Data will be made available on request.

Acknowledgements

We appreciate the support of our Departments and the Pittsburgh Institute for Neurodegenerative Disease (PIND) at the University of Pittsburgh, United States and the many helpful suggestions from colleagues therein. In particular we are grateful for assistance and advice from Dr. Stacey J. Sukoff Rizzo. We are grateful to the National Institutes of Health, United States for funding this research project via R03 NS119664 (MJP), R01 HD105311 (MJP), R01 HD104346 (MJP), T32 GM133332 (TDM), and U01 AA020889 (GEH). This project used the UPMC Hillman Cancer Center and Tissue and Research Pathology/Pitt Biospecimen Core, United States shared resource which is supported in part by award P30CA047904.

Appendix A. Supplementary data

Supplementary data to this article can be found online at https://doi.org/10.1016/j.crneur.2022.100062.

References

Arya, R., Lalloz, M.R., Bellingham, A.J., Layton, D.M., 1997. Evidence for founder effect of the Glu104Asp substitution and identification of new mutations in triosephosphate isomerase deficiency. Hum. Mutat. 10 (4), 290–294. https://doi.org/10.1002/(SICI)1098-1004(1997)10, 4<290::AID-HUMU4>3.0.CO;2-L.

Cabrera, N., Torres-Larios, A., Garcia-Torres, I., Enriquez-Flores, S., Perez-Montfort, R., 2018. Differential effects on enzyme stability and kinetic parameters of mutants related to human triosephosphate isomerase deficiency. Biochim. Biophys. Acta Gen. Subj. 1862 (6), 1401–1409. https://doi.org/10.1016/j.bbagen.2018.03.019.

Concordet, J.P., Haeussler, M., 2018. CRISPOR: intuitive guide selection for CRISPR/Cas9 genome editing experiments and screens. Nucleic Acids Res. 46 (W1), W242–W245. https://doi.org/10.1093/nar/gky354.

Conway, A.J., Brown, F.C., Hortle, E.J., Burgio, G., Foote, S.J., Morton, C.J., Curtis, D.J., 2018. Bone marrow transplantation corrects haemolytic anaemia in a novel ENU mutagenesis mouse model of TPI deficiency. Dis Model Mech 11 (5). https://doi.org/10.1242/dmm.034678.

De La Mora-De La Mora, I., Torres-Larios, A., Mendoza-Hernandez, G., Enriquez-Flores, S., Castillo-Villanueva, A., Mendez, S.T., Reyes-Vivas, H., 2013. The E104D mutation increases the susceptibility of human triosephosphate isomerase to proteolysis. Asymmetric cleavage of the two monomers of the homodimeric enzyme. Biochim. Biophys. Acta 1834 (12), 2702–2711. https://doi.org/10.1016/j.bbapap.2013.08.012.

Fogle, K.J., Smith, A.R., Satterfield, S.L., Gutierrez, A.C., Hertzler, J.I., McCardell, C.S., Palladino, M.J., 2019. Ketogenic and anaplerotic dietary modifications ameliorate seizure activity in Drosophila models of mitochondrial encephalomyopathy and glycolytic enzymopathy. Mol. Genet. Metabol. 126 (4), 439–447. https://doi.org/10.1016/j.ymgme.2019.01.008.

Hollan, S., Fujii, H., Hirono, A., Hirono, K., Karro, H., Miwa, S., Inselt-Kovacs, M., 1993. Hereditary triosephosphate isomerase (TPI) deficiency: two severely affected brothers one with and one without neurological symptoms. Hum. Genet. 92 (5), 486–490. https://doi.org/10.1007/BF00216456.

Hough, S.H., Ajetunmobi, A., Brody, L., Humphryes-Kirilov, N., Perello, E., 2016. Desktop genetics. Per Med 13 (6), 517–521. https://doi.org/10.2217/pme-2016-0068.

Hrizo, S.L., Eicher, S.L., Myers, T.D., McGrath, I., Wodrich, A.P.K., Venkatesh, H., Palladino, M.J., 2021. Identification of protein quality control regulators using a Drosophila model of TPI deficiency. Neurobiol. Dis. 152, 105299 https://doi.org/10.1016/j.nbd.2021.105299.

Hrizo, S.L., Palladino, M.J., 2010. Hsp70- and Hsp90-mediated proteasomal degradation underlies TPI sugarkill pathogenesis in Drosophila. Neurobiol. Dis. 40 (3), 676–683. https://doi.org/10.1016/j.nbd.2010.08.011.

National Research Council, 2011. Guide for the Care and Use of Laboratory Animals, eighth ed. The National Academies Press, Washington, DC.

Orosz, F., Olah, J., Ovadi, J., 2006. Triosephosphate isomerase deficiency: facts and doubts. IUBMB Life 58 (12), 703–715. https://doi.org/10.1080/15216540601115960.

Orosz, F., Olah, J., Ovadi, J., 2009. Triosephosphate isomerase deficiency: new insights into an enigmatic disease. Biochim. Biophys. Acta 1792 (12), 1168–1174. https://doi.org/10.1016/j.bbadis.2009.09.012.

Pretsch, W., 2009. Triosephosphate isomerase activity-deficient mice show haemolytic anaemia in homozygous condition. Genet Res (Camb) 91 (1), 1–4. https://doi.org/10.1017/S0016672308009944.

Ralser, M., Heeren, G., Breitenbach, M., Lehrach, H., Krobitsch, S., 2006. Triose phosphate isomerase deficiency is caused by altered dimerization–not catalytic inactivity–of the mutant enzymes. PLoS One 1, e30. https://doi.org/10.1371/journal.pone.0000030.

Renaud, J.B., Boix, C., Charpentier, M., De Cian, A., Cochennec, J., Duvernois-Berthet, E., Giovannangeli, C., 2016. Improved genome editing efficiency and flexibility using modified oligonucleotides with TALEN and CRISPR-cas9 nucleases. Cell Rep. 14 (9), 2263–2272. https://doi.org/10.1016/j.celrep.2016.02.018.

Rodriguez-Almazan, C., Arreola, R., Rodriguez-Larrea, D., Aguirre-Lopez, B., de Gomez-Puyou, M.T., Perez-Montfort, R., Torres-Larios, A., 2008. Structural basis of human triosephosphate isomerase deficiency: mutation E104D is related to alterations of a conserved water network at the dimer interface. J. Biol. Chem. 283 (34), 23254–23263. https://doi.org/10.1074/jbc.M802145200.

Roland, B.P., Richards, K.R., Hrizo, S.L., Eicher, S., Barile, Z.J., Chang, T.C., Palladino, M. J., 2019. Missense variant in TPI1 (Arg189Gln) causes neurologic deficits through structural changes in the triosephosphate isomerase catalytic site and reduced enzyme levels in vivo. Biochim. Biophys. Acta, Mol. Basis Dis. 1865 (9), 2257–2266. https://doi.org/10.1016/j.bbadis.2019.05.002.

Schneider, A.S., Valentine, W.N., Hattori, M., Heins Jr., H.L., 1965. Hereditary hemolytic anemia with triosephosphate isomerase deficiency. N. Engl. J. Med. 272, 229–235. https://doi.org/10.1056/NEJM196502042720503.

Schneider, C.A., Rasband, W.S., Eliceiri, K.W., 2012. NIH Image to ImageJ: 25 years of image analysis. Nat. Methods 9 (7), 671–675. https://doi.org/10.1038/nmeth.2089.

Segal, J., Mulleder, M., Kruger, A., Adler, T., Scholze-Wittler, M., Becker, L., Ralser, M., 2019. Low catalytic activity is insufficient to induce disease pathology in triosephosphate isomerase deficiency. J. Inherit. Metab. Dis. 42 (5), 839–849. https://doi.org/10.1002/jimd.12105.

Seigle, J.L., Celotto, A.M., Palladino, M.J., 2008. Degradation of functional triose phosphate isomerase protein underlies sugarkill pathology. Genetics 179 (2), 855–862. https://doi.org/10.1534/genetics.108.087551.

Shi, Y., Vaden, D.L., Ju, S., Ding, D., Geiger, J.H., Greenberg, M.L., 2005. Genetic perturbation of glycolysis results in inhibition of de novo inositol biosynthesis. J. Biol. Chem. 280 (51), 41805–41810. https://doi.org/10.1074/jbc.M505181200.

VanDemark, A.P., Hrizo, S.L., Eicher, S.L., Kowalski, J., Myers, T.D., Pfeifer, M.R., Palladino, M.J., 2022. Itavastatin and resveratrol increase triosephosphate isomerase protein in a newly identified variant of TPI deficiency. Dis Model Mech 15 (5). https://doi.org/10.1242/dmm.049261.

Vogt, A., Eicher, S.L., Myers, T.D., Hrizo, S.L., Vollmer, L.L., Meyer, E.M., Palladino, M.J., 2021. A high-content screening assay for small molecules that stabilize mutant triose phosphate isomerase (TPI) as treatments for TPI deficiency. SLAS Discov 26 (8), 1029–1039. https://doi.org/10.1177/24725552211018198.